Development of preferred orientation in polycrystalline NaCl-structure δ-TaN layers grown by reactive magnetron sputtering: Role of low-energy ion surface interactions

C.-S. Shin, D. Gall, Y.-W. Kim, N. Hellgren, I. Petrov, and J. E. Greene[a)]
Department of Materials Science and Frederick Seitz Materials Research Laboratory, University of Illinois, 104 South Goodwin, Urbana, Illinois 61801

(Received 15 July 2002; accepted 2 August 2002)

We have investigated the effects of low-energy ion irradiation on texture evolution during growth of B1–NaCl-structure polycrystalline δ-TaN layers on SiO_2 by ultra-high-vacuum reactive magnetron sputter deposition at 350 °C in mixed Ar+15% N_2 discharges. In parallel sets of experiments, the ion-to-metal flux ratio J_i/J_{Ta} was varied from 1.3 to 10.7 while maintaining the incident ion energy E_i constant at 20 eV, and E_i was varied from 8.5 to 30 eV with $J_i/J_{Ta}=10.7$. All TaN layers, irrespective of J_i/J_{Ta} or E_i, were overstoichiometric with N/Ta$=1.13\pm0.03$. Layers grown with $E_i=30$ eV are multiphase consisting of hexagonal ε-TaN and δ-TaN, while those grown with $E_i \leqslant 20$ eV are single-phase δ-TaN. With $E_i=8.5$ eV, the δ-TaN layers have a mixed 111/002/022/113 texture, even for film thicknesses t up to 500 nm. In contrast, δ-TaN layers deposited with $E_i=20$ eV initially exhibit competitive texture evolution until a single texture dominates at $t \gtrsim 200$ nm. The preferred orientation of 500-nm-thick $E_i=20$ eV layers can be selectively and continuously varied from predominantly 111 to nearly complete 002 by increasing J_i/J_{Ta} from 1.3 to $\geqslant$ 7.4. The change in texture is primarily due to an increased steady-state atomic N coverage, resulting from collisionally induced dissociative chemisorption of incident energetic N_2^+ ions, with increasing J_i/J_{Ta}. 111-oriented δ-TaN layers are underdense with both inter- and intracolumnar porosity and a tensile stress of $\simeq$ 1.4 GPa, while 002-oriented layers are fully dense and have small compressive stresses, $\lesssim$ 0.7 GPa. © *2002 American Institute of Physics.*
[DOI: 10.1063/1.1510558]

I. INTRODUCTION

Polycrystalline B1–NaCl-structure δ-TaN thin films are presently used in a variety of applications including hard wear-resistant coatings on tools, diffusion barriers in integrated circuits, resistors, and mask layers for x-ray lithography. The physical properties of δ-TaN layers, and hence their suitability for these applications, are strongly affected by microstructural attributes such as grain size and shape (equiaxed versus columnar), porosity, defect density, and texture. The latter dependence stems from the fact that cubic transition-metal (TM) nitrides are strongly elastically anisotropic. Thus, the performance of δ-TiN, by far the most widely studied TM nitride to date, in hard wear-resistant coating[1,2] and microelectronic diffusion barrier[3] applications has been shown to depend strongly on preferred orientation.

Here, we focus on texture control during the growth of cubic δ-TaN layers. We anticipate that the evolution of microstructure in TaN thin films will be extremely sensitive to growth conditions due to the richness of the Ta–N system. In addition to the equilibrium phases of bcc α-Ta, solid-solution α-Ta(N), hexagonal γ-Ta_2N, and hexagonal ε-TaN, a large variety of under- and overstoichiometric metastable phases have been reported. These include tetragonal β-Ta, bcc β-Ta(N), hexagonal $TaN_{0.8}$, hexagonal WC-structure θ-TaN, NaCl-structure δ-TaN, hexagonal Ta_5N_6, tetragonal Ta_4N_5, and orthorhombic Ta_3N_5.[4,5]

The majority of TM nitride applications require low film growth temperatures, $T_s \leqslant 450$ °C (i.e., $T_s/T_m \leqslant 0.24$ for TaN where T_m is the melting point in K), and in almost all cases the layers are deposited by magnetron sputter deposition. Low-temperature growth is necessary, for example, to avoid overtempering of steel cutting-tool substrates and exceeding the tight thermal budgets associated with Si-based device fabrication. Consequently, ion-assisted film growth, in which the ion-energy E_i and the incident ion-to-metal atom flux ratio J_i/J_{Me} are fundamental parameters, is often employed to control TM nitride film microstructure. Momentum transfer to the lattice during deposition can have a large, and often dominant, influence on adatom mobilities, film nucleation rates, solute solubilities, and residual stresses.[6,7] While E_i is easily controlled during conventional magnetron sputtering through the use of an external substrate bias, J_i/J_{Me} cannot be varied independently. Thus, most studies of the effects of ion irradiation during film growth have concentrated exclusively on the role of E_i, with J_i/J_{Me} either constant or uncontrolled and typically of order 0.5–1. The use of E_i values significantly above bulk lattice displacement thresholds, $\gtrsim$20 eV depending upon the materials system (i.e., ion mass and layer composition), leads to film densification and a less pronounced columnar microstructure compared to films grown with lower ion energies. However, these advantages

[a)]Electronic mail: greene@mrl.uiuc.edu

 © 2002 American Institute of Physics

Downloaded 31 Oct 2002 to 128.113.37.128. Redistribution subject to AIP license or copyright, see http://ojps.aip.org/japo/japcr.jsp

extract a steep price. In the case of TiN and $Ti_{1-x}Al_xN$ growth, for example, the use of incident N_2^+ energies E_i >25 eV results in trapping of accelerated ions, residual lattice defects, and the development of very high compressive stresses.[8–10]

Petrov *et al.*[11] demonstrated that external Helmholtz coils with Fe pole pieces can be used to controllably unbalance the magnetic circuit in a magnetron sputtering system through the addition of a uniform axial magnetic field between the target and the substrate. The unbalanced field allows the crystal grower to shape the discharge near the substrate and provides independent control of the energy and flux of ions incident at the growing film with negligible effect on the target sputtering rate. This opened the way for systematic studies of the effects of low-energy ion irradiation during film growth in which it was observed that the reaction paths associated with independently varying E_i and J_i/J_{Me} are quite different.[8–13] In fact, varying J_i/J_{Me} over a wide range, while maintaining $E_i \leqslant 20$ eV, during magnetron sputter deposition has been shown to be an effective method for controlling the microstructural evolution of polycrystalline NaCl-structure TiN,[12,13] $Ti_{0.5}Al_{0.5}N$,[10,14] and ScN,[15] while introducing negligible concentrations of residual ion-induced defects and residual stress.

In this article, we summarize the results of an investigation of low-energy ion irradiation effects on microstructure and texture evolution during deposition of metastable B1–NaCl-structure δ-TaN layers. The films were grown by ultrahigh-vacuum (UHV) magnetically unbalanced reactive magnetron sputter deposition on amorphous SiO_2 at $T_s = 350\,°C$ in mixed Ar+15% N_2 discharges at a total pressure of 20 mTorr. The ion-to-Ta atom flux ratio J_i/J_{Ta} was varied from 1.3 to 10.7 while maintaining $E_i = 20$ eV, and E_i was varied from 8.5 to 30 eV with $J_i/J_{Ta} = 10.7$. All TaN layers, irrespective of J_i/J_{Ta} and E_i, were overstoichiometric with N/Ta$=1.13\pm0.03$. The use of $E_i = 8.5$ eV ion irradiation during deposition, even with the very high ion flux ratio of $J_i/J_{Ta} = 10.7$, was found to have no significant effect on orientation development; all films exhibited a mixed 111/002/022/113 texture. Increasing E_i to 30 eV, however, results in a multiphase structure consisting of cubic δ-TaN and hexagonal ε-TaN.

In contrast to the above results, the use of $E_i = 20$ eV ion irradiation during film growth has a dramatic and positive effect on both microstructural and texture evolution. All films are single-phase δ-TaN in which strong preferred orientation develops in a competitive kinetically limited mode until a single texture, controlled by the ion-to-metal flux ratio, dominates at thicknesses $t \gtrsim 200$ nm. Increasing J_i/J_{Ta} from 1.3 to $\geqslant 7.4$ continuously changes the preferred orientation of 500-nm-thick $E_i = 20$ eV layers from 111 to 002. Layers grown at low J_i/J_{Ta} values initially exhibit a mixed 111/002 texture, which slowly evolves with film thickness into a nearly complete 111 preferred orientation. However, the films are underdense with both inter- and intracolumnar porosity, resulting in a tensile stress of +1.4 GPa. 002 δ-TaN layers, grown with high J_i/J_{Ta} values, are fully dense and have relatively small compressive stresses ranging from -0.6 GPa with $J_i/J_{Ta} = 7.4$ to -0.7 GPa with $J_i/J_{Ta} = 10.7$. The relaxed lattice constant of δ-$TaN_{1.13}$ is 0.4353 ± 0.0004 nm.

II. EXPERIMENTAL PROCEDURE

All TaN films were grown in a load-locked multichamber UHV stainless-steel dc magnetron sputter deposition system described in detail in Ref. 11. The system is equipped with a pair of external Helmholtz coils with Fe pole pieces creating a uniform axial magnetic field B_{ext} between the target and the substrate that can be varied between -180 and $+180$ G. The base pressure in the deposition chamber, achieved using a 500 $1\,s^{-1}$ turbomolecular pump, is 5×10^{-10} Torr (7×10^{-8} Pa). A water-cooled 6.35-cm-diam Ta target with a purity of 99.97% was mounted 10 cm from the substrate holder and sputtering was carried out in a mixed atmosphere consisting of 85% Ar (99.9999% pure) and 15% N_2 (99.999%) at a total pressure of 20 mTorr (2.67 Pa). During deposition, the pressure was monitored by a capacitance manometer and maintained constant with automatic mass-flow controllers.

The magnetron was operated in constant power mode at 150 W yielding a discharge voltage of 340 ± 7 V and a current of 0.46 ± 0.01 A with a fully nitrided Ta target. These deposition conditions resulted in a film growth rate R, obtained from both microstylus profilometry measurements and cross-sectional transmission electron microscopy (XTEM), of 2.55 $\mu m\,h^{-1}$. R was not affected by changes in J_i/J_{Ta} and E_i over the ranges used in this investigation. TaN film thicknesses were 50–500 nm.

Monte Carlo simulations carried out using the TRIM90 computer code[16] showed that for 340 eV Ar^+, N_2^+, and N^+ ions bombarding a nitrided Ta target, the reflection coefficients and average reflected energies are 0.17 and 56 eV for Ar^+, 0.21 and 58 eV for N_2^+, and 0.22 and 123 eV for N^+. The thermalization distances in a 20 mTorr Ar discharge were estimated using persistence theory[17] with energy-dependent cross sections[18] to be <6.5 cm for energetic reflected Ar, N_2, and N and even less for Ta atoms, which are sputter ejected with an average energy of 34 eV. Thus, under the present deposition conditions, a majority of both the sputtered species and the energetic neutrals backscattered from the target are thermalized during transport and contribute little to the flux of energetic particles incident at the substrate.

Plasma characteristics in the vicinity of the substrate during film growth were determined from Langmuir probe measurements following the procedures described in Ref. 11. A 6-mm-diam stainless-steel disk mounted in a through-hole drilled in the center of a substrate platen was used to measure the ion flux density J_i at the growing film surface. The surface of the probe was located at the same level as the substrate surface and was electrically isolated from the platen by a vacuum gap of 0.25 mm. To minimize edge effects, the probe and substrate platen were maintained at the same potential with respect to the grounded chamber. The plasma and floating potentials were obtained from the current–voltage characteristics of a smaller cylindrical probe, 5 mm long by 0.4 mm in diameter, situated 6 mm above the substrate sur-

Downloaded 31 Oct 2002 to 128.113.37.128. Redistribution subject to AIP license or copyright, see http://ojps.aip.org/japo/japcr.jsp

face. E_i was controlled through the substrate bias V_s while B_{ext} was used to independently vary J_i/J_{Ta}.

The substrates were 400-nm-thick amorphous-SiO_2 layers produced by thermally oxidizing $10\times10\times0.5\ mm^3$ Si(001) wafers. Substrate cleaning consisted of successive rinses in ultrasonic baths of trichloroethane, acetone, methanol, and deionized water. The substrates were then blown dry in dry N_2, mounted on resistively heated Ta platens using Mo clips, and inserted into the sample introduction chamber for transport to the growth chamber where they were thermally degassed at 500 °C for 1 h. Immediately prior to initiating deposition, the target was sputter etched for 5 min with a shutter shielding the substrate. Film growth temperatures T_s, including the contribution due to plasma heating, were measured with a pyrometer calibrated by a thermocouple bonded to a TaN-coated Si substrate. Following deposition, the samples were allowed to cool below 100 °C before transferring them to the load-lock chamber, which was then vented with dry N_2.

Film compositions were determined by Rutherford backscattering spectrometry (RBS) using a 2 MeV He^+ probe beam with a scattering angle of 150° and a total accumulated ion dose of 100 μC. Backscattered spectra were analyzed using the RUMP simulation program.[19] The uncertainty in determining the N/Ta ratio is less than ±0.03. Combining the results of the probe measurements with RBS data for the total number of deposited Ta atoms yields values for the ion-to-Ta flux ratios J_i/J_{Ta} incident at the substrate.

Microstructure and phase determinations in as-deposited TaN films were carried out using a combination of x-ray diffraction (XRD), plan-view TEM, and XTEM. ω–2θ and glancing-angle XRD (GA-XRD) scans were obtained in the powder diffraction mode with a resolution of 0.01° 2θ, while pole figures were acquired using a four-circle Philips X-pert diffractometer. TEM and XTEM analyses were performed in a Philips CM12 microscope operated at 120 kV. Plan-view specimens were prepared by mechanically thinning the samples from the backside with SiC to a thickness of $\simeq$ 30 μm. Final thinning to electron transparency was accomplished by ion milling using a 5 keV Ar^+ ion beam incident at 8°. Cross-sectional specimens were prepared by gluing two samples film to film and then cutting vertical sections, which were ground and milled in a similar manner to that of the plan-view samples, but from both sides.

III. EXPERIMENTAL RESULTS

A. Plasma probe measurements

Varying B_{ext} during reactive sputter deposition of TaN dramatically alters the ion flux J_i incident at the growing film. The probe measurements summarized in Fig. 1 show that J_i increases from 3.9×10^{15} to $3.2\times10^{16}\ cm^{-2}\ s^{-1}$ (0.62 to 5.10 mA cm^{-2}) as B_{ext} is increased from -60 to $+180$ G. Changes in B_{ext} over this range, however, had very little effect on the overall impedance of the magnetron discharge. At a constant target power of 150 W, the discharge voltage increases from 334 V at $B_{ext}=-60$ G to 348 V at $+180$ G with no measurable change in the target sputtering rate; J_{Ta} remains constant at $3.0\times10^{15}\ cm^{-2}\ s^{-1}$. Thus, as shown in

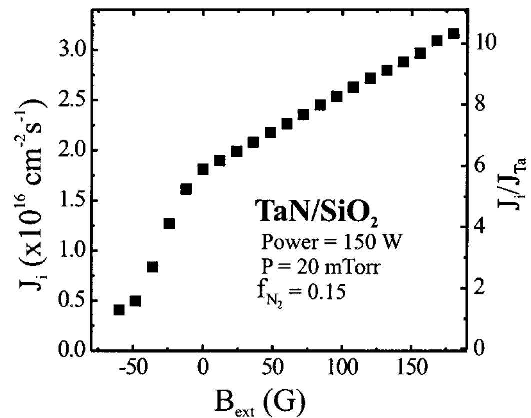

FIG. 1. Saturation ion current density J_i and ion-to-Ta flux ratio J_i/J_{Ta} at the substrate as a function of the external magnetic field B_{ext} during magnetically unbalanced reactive magnetron sputter deposition of TaN in Ar $+15\%$ N_2 discharges at a total pressure of 20 mTorr.

Fig. 1, J_i/J_{Ta} can be varied over nearly an order of magnitude, from 1.3 to 10.7. The corresponding changes in the plasma potential V_p and floating potential V_f range from $+0.3$ to -17.5 V and -13.4 to -26.0 V, respectively.

From previous double-modulated glow discharge mass spectrometry measurements,[20] the composition of the ion flux incident at the substrate during reactive magnetron sputtering under the present experimental conditions is 93% Ar^+, 3% Ar^{2+}, 2.8% $N_2{}^+$, and 1.1% N^+. The vast majority of the ions incident at the growing film experience the full sheath potential, $E_i\simeq e(|V_s-V_p|)$, where V_s is the negative substrate bias ($V_s=V_f$, if no bias is applied), since the mean-free paths for Ar^+ and $N_2{}^+$ charge exchange collisions[18] are $\simeq$8 mm, more than an order of magnitude large than the sheath width, which is estimated from the Child–Langmuir equation[21] to be 0.2–0.5 mm.

B. TaN stoichiometry, microstructure, and texture

Metastable cubic δ-TaN exhibits a wide single-phase field with a N/Ta ratio extending from 0.94 to 1.37,[22] while the equilibrium low-temperature hexagonal ε-TaN phase has a narrower field, 0.96–1.0.[23] In the present experiments, all TaN films grown at $T_s=350$ °C were found to be overstoichiometric with N/Ta$=1.13\pm0.03$; film stoichiometry was not significantly affected by either J_i/J_{Ta} or E_i. However, we note that N/Ta varies strongly with T_s, ranging from 1.22 ± 0.03 with $T_s=100$ °C to 1.08 ± 0.03 at $T_s=600$ °C.

Figures 2(a) and 2(b) are typical XRD ω–2θ and GA-XRD 2θ scans, respectively, from 500-nm-thick $T_s=350$ °C layers grown as a function of E_i with $J_i/J_{Ta}=10.7$. The ω–2θ scan from the 30 eV layer [Fig. 2(a)] consists of (110) and (220) hexagonal ε-TaN peaks centered at $2\theta=34.92°$ and 73.45°, as well as (111) and (002) δ-TaN peaks at 35.35° and 41.21°. The corresponding $E_i=30$ eV GA-XRD 2θ scan in Fig. 2(b) also contains both ε-and δ-phase TaN reflections. The (002) δ-TaN peak at $2\theta=41.43°$ is the dominant ω–2θ XRD feature obtained from the $E_i=20$ eV layer, while the GA-XRD scan contains, in addition, (111) and (113) δ-TaN peaks at 35.80° and 71.98°. Figures 2(a) and 2(b) show that the layer grown at E_i

Downloaded 31 Oct 2002 to 128.113.37.128. Redistribution subject to AIP license or copyright, see http://ojps.aip.org/japo/japcr.jsp

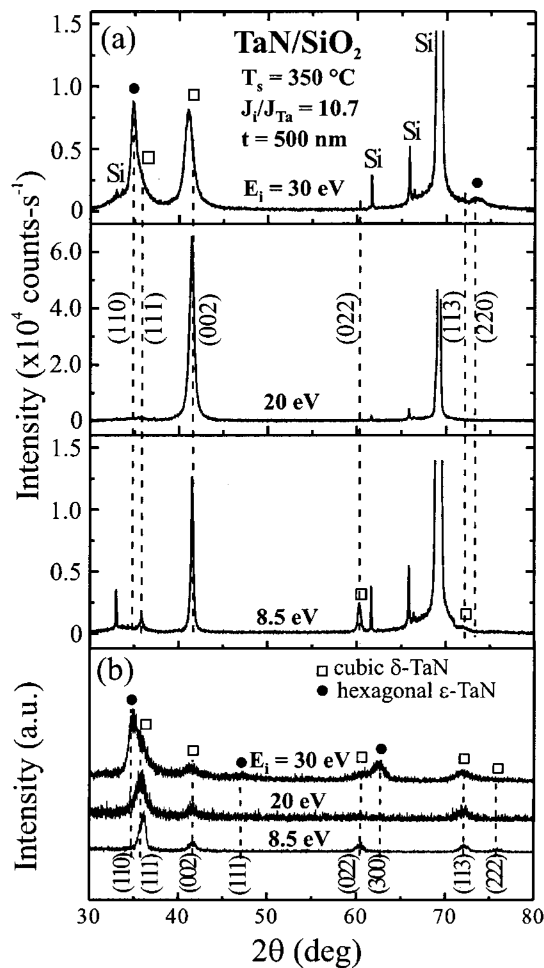

FIG. 2. (a) XRD ω–2θ and (b) GA-XRD 2θ scans from 500-nm-thick TaN layers deposited on amorphous SiO_2 at 350 °C as a function of the incident ion energy E_i with J_i/J_{Ta} maintained constant at 10.7.

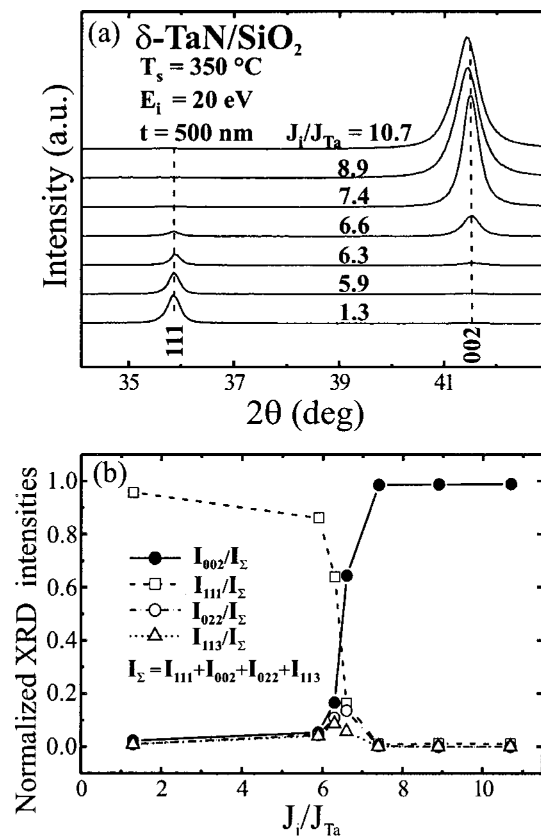

FIG. 3. (a) XRD ω–2θ scans from 500-nm-thick δ-TaN layers deposited on amorphous SiO_2 at 350 °C as a function of J_i/J_{Ta} with $E_i = 20$ eV. (b) Normalized intensities of the (111), (002), (022), and (113) XRD peaks in (a) as a function of J_i/J_{Ta}.

$=8.5$ eV consists of (111), (002), (022), and (113) oriented grains. The relatively low peak intensities suggest that an ion energy of 8.5 eV is too small, even with the high ion-to-metal flux ratio $J_i/J_{Ta} = 10.7$, to have a significant effect on film texture development. Thus, we concentrated on $E_i = 20$ eV to investigate the effect of ion flux on δ-TaN texture evolution.

ω–2θ and GA-XRD scans from 500-nm-thick TaN layers grown at $T_s = 350°$C with $E_i = 20$ eV and J_i/J_{Ta} values ranging from 1.3 to 10.7 contain predominantly (111) and/or (002) δ-TaN reflections; no other phases were detected. Typical ω–2θ results are shown in Fig. 3(a). Films grown with high-flux ratios ($J_i/J_{Ta} \geqslant 7.4$) exhibit a complete 002 texture while those grown with $J_i/J_{Ta} \leqslant 6.3$ have a strong 111 preferred orientation with small volume fractions of 002, 022, and 113 grains. XRD pole figures reveal, in addition, that all diffraction peak maxima are aligned along the growth direction and that peak intensities are azimuthally symmetric.

The above results clearly demonstrate that the incident ion-to-metal flux ratio can be used to selectively and controllably vary the preferred orientation of δ-TaN films from predominately 111 to 002. This is illustrated in Fig. 3(b) by plotting normalized *hkl* XRD peak intensities ($I_{hkl}/[I_{111} + I_{002} + I_{022} + I_{113}]$) as a function of J_i/J_{Ta}. The minimum ion-to-metal flux ratio required to obtain an essentially complete 002 texture for δ-TaN, $J_i/J_{Ta} \simeq 7.5$, is larger than that required for TiN (Refs. 12 and 13) and $Ti_{0.5}Al_{0.5}N$ (Refs. 10 and 14) layers for which the critical ratio was found to be $\simeq 4$. This is the case even though the latter experiments were carried out in pure N_2 discharges for which the dominant ion, N_2^+, has a lower mass (28 amu) than Ar^+ (39.95 amu), the primary ion in the present experiments. We attribute this to the much larger mass of Ta (180.95 amu), compared to Ti (47.9 amu) and Al (27 amu), requiring increased energy deposition via momentum transfer from incident ions in order to enhance cation surface mobilities.

The (002) peak positions in Fig. 3(a) are shifted to lower 2θ angles (i.e., larger lattice parameters $a_\perp$ along the growth direction) with increasing $J_i/J_{Ta} \geqslant 6.6$ while the (111) peak positions in the layers grown with low J_i/J_{Ta} ($\leqslant 6.3$) remain approximately constant at $2\theta \simeq 35.8°$, corresponding to $a_\perp^{111} = 0.4344$ nm. $a_\perp^{002}$ increases from 0.4350 nm with $J_i/J_{Ta} = 6.6$ to 0.4361 nm with $J_i/J_{Ta} = 10.7$, indicating that the films are under increasing compressive stress.

All δ-TaN layers were analyzed using the XRD $\sin^2\psi$ technique, where $\psi = (\theta - \alpha)$ with α being the incidence angle of the x-ray beam, in order to estimate residual in-plane stresses σ as well as to determine the relaxed δ-TaN lattice constant a_o. The lattice parameter a_ψ was obtained for each sample using the (111), (113), (133), (024), and (224) diffraction peaks for 111-textured layers (J_i/J_{Ta}

Downloaded 31 Oct 2002 to 128.113.37.128. Redistribution subject to AIP license or copyright, see http://ojps.aip.org/japo/japcr.jsp

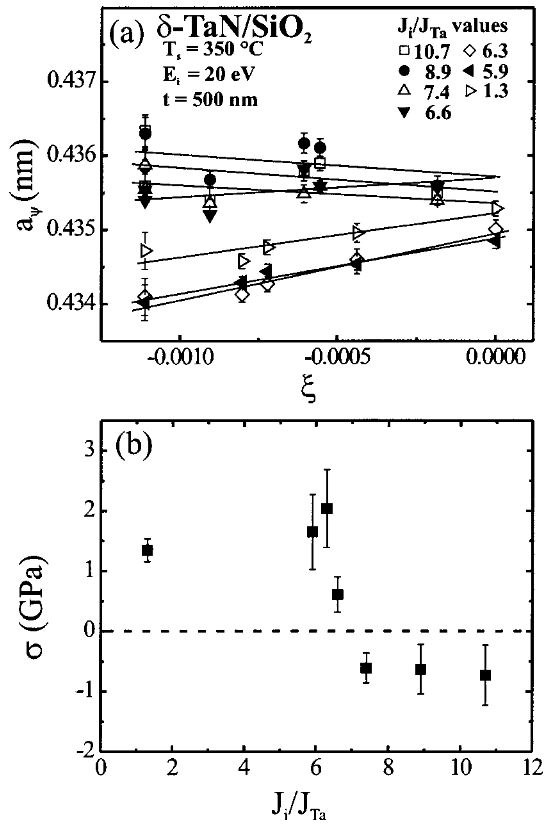

FIG. 4. (a) Plot of a_ψ vs ξ [see Eq. (3)] and (b) residual stress values σ determined from $\sin^2\psi$ XRD measurements of 500-nm-thick δ-TaN layers deposited on amorphous SiO_2 at 350 °C as a function of J_i/J_{Ta} with E_i =20 eV.

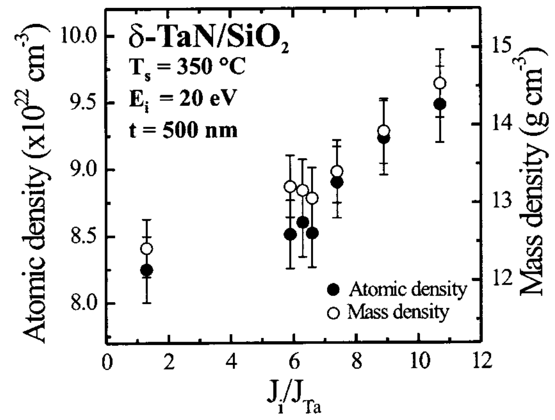

FIG. 5. Atomic and mass densities of 500-nm-thick δ-TaN layers deposited on amorphous SiO_2 at 350 °C as a function of J_i/J_{Ta} with E_i=20 eV.

$\leqslant 6.3$) and the (002), (113), (004), (204), (224), and (115) peaks for 002-oriented layers ($J_i/J_{Ta}\geqslant 6.6$). The data were recorded in 2θ and ψ values were determined from the relationships

$$\cos\psi=\frac{h+k+l}{[3(h^2+k^2+l^2)]^{1/2}}, \tag{1}$$

for 111 layers and

$$\cos\psi=\frac{1}{(h^2+k^2+l^2)^{1/2}}, \tag{2}$$

for 002 layers. The in-plane stress σ and bulk lattice constant a_o are related to measured a_ψ values through the equation

$$a_\Psi=a_o+a_o\sigma\left(\frac{(1+\nu_{hkl})}{E_{hkl}}\sin^2\psi-2\frac{\nu_{hkl}}{E_{hkl}}\right)=a_o(1+\sigma\xi), \tag{3}$$

where ν_{hkl} and E_{hkl} are the Poisson ratio and elastic modulus of the film in the $[hkl]$ direction.

We are unaware of any published data for either the Poisson ratio or the orientation dependence of the elastic modulus of δ-TaN. Thus, we have used the elastic modulus of single-crystal δ-TaN(002), $E=450$ GPa,[24] and taken ν to be 0.25,[25] irrespective of orientation. We estimate that the resulting maximum uncertainties in determining σ and a_o are ±0.3 GPa and ±0.00005 nm, respectively. Measured a_ψ vs ξ values as a function of J_i/J_{Ta} are plotted in Fig. 4(a) with residual stresses calculated from Eq. (3) given in Fig. 4(b). σ is tensile in 111-textured layers (low J_i/J_{Ta} values) and slightly compressive in 002-oriented films (high J_i/J_{Ta} values). Overall, the residual stress ranges from +1.4 GPa with $J_i/J_{Ta}=1.3$ to -0.7 GPa with $J_i/J_{Ta}=10.7$. The film/substrate differential thermal contraction stress due to cooling from $T_s=350\,°C$ to room temperature is given by $\sigma_T=[E_{TaN}/(1-\nu_{TaN})](\alpha_{TaN}-\alpha_{Si})\Delta T$, where $\alpha_{TaN}=8.0\times10^{-6}\ K^{-1}$ (Ref. 26) and $\alpha_{Si}=2.59\times10^{-6}\ K^{-1}$ (Ref. 27) are the thermal expansion coefficients of TaN and Si (the oxide layer is too thin to have an effect). Thus, $\sigma_T\simeq+1.05$ GPa tensile.

The relaxed lattice constant for polycrystalline δ-$TaN_{1.13}$ layers was determined from Eq. (3) to be $a_o=0.4353\pm0.0004$ nm, which is within the range of previously reported lattice constant values, 0.433–0.442 nm, obtained from polycrystalline δ-TaN_x layers and bulk powder samples.[28–30]

Figure 5 shows the change in δ-TaN atomic and mass densities, determined from a combination of RBS analyses and film thickness measurements, as a function of J_i/J_{Ta} for $E_i=20$ eV δ-TaN layers, corresponding to the samples in Fig. 3. The atomic density increases from $8.3\pm0.3\times10^{22}\ cm^{-3}$ with $J_i/J_{Ta}=1.3$ to near-theoretical density, $9.85\times10^{22}\ cm^{-3}$, with $J_i/J_{Ta}\geqslant 8.9$. Thus, increasing J_i/J_{Ta}, with $E_i=20$ eV, controls not only film texture but film density as well.

Figures 6(a) and 6(b) are plan-view TEM micrographs of $E_i=20$ eV δ-TaN layers grown with the lowest and the highest ion fluxes. The absence of Moiré fringes indicates that both films have a columnar microstructure. The 111-textured layer shown in Fig. 6(a) ($J_i/J_{Ta}=1.3$) exhibits an underdense structure with open grain boundaries. In contrast, the 002-textured layer grown with $J_i/J_{Ta}=10.7$ [Fig. 6(b)] appears fully dense, consistent with the results in Fig. 5.

XTEM images from the 111-textured sample corresponding to Fig. 6(a) are presented in Fig. 7. Lower- and higher-magnification [Figs. 7(a) and 7(b)] bright-field micrographs from the upper region of the film clearly show that the microstructure is columnar and underdense with both inter- as well as intracolumnar voids. In addition, the surface is very irregular with a root-mean-square (rms) roughness of

Downloaded 31 Oct 2002 to 128.113.37.128. Redistribution subject to AIP license or copyright, see http://ojps.aip.org/japo/japcr.jsp

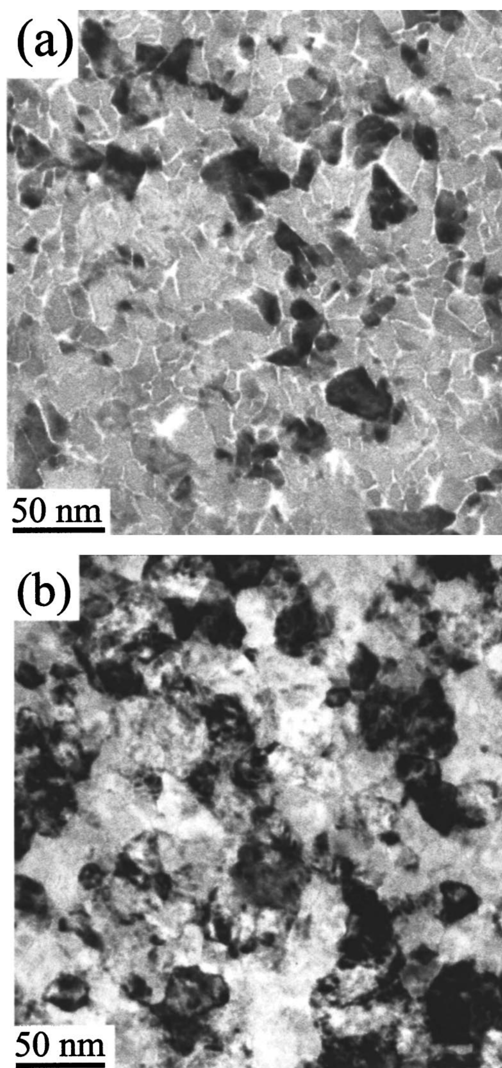

FIG. 6. Bright-field plan-view TEM images from 500-nm-thick δ-TaN layers deposited on amorphous SiO_2 at 350 °C with $E_i = 20$ eV: (a) $J_i/J_{Ta} = 1.3$ and (b) $J_i/J_{Ta} = 10.7$.

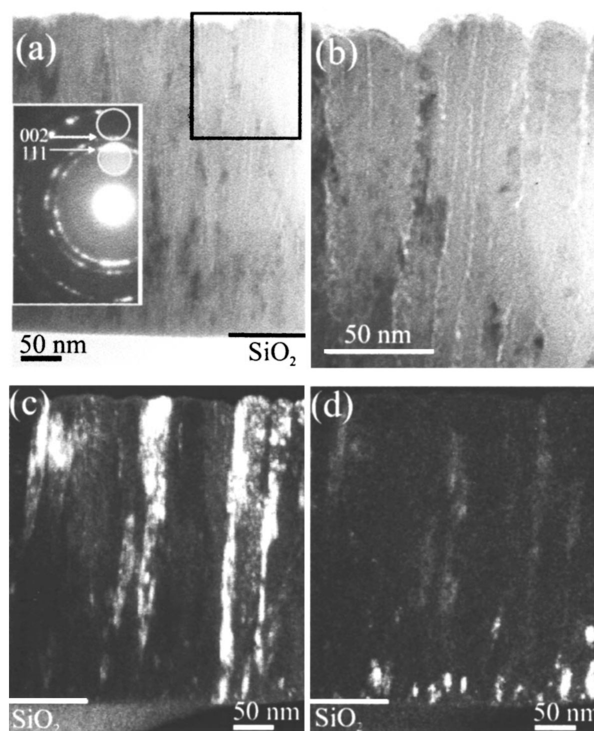

FIG. 7. (a) Bright-field XTEM micrograph and corresponding SAED pattern obtained from the sample corresponding to Fig. 6(a). (b) Higher-magnification image of the region outlined by the black box in (a). (c) and (d) are dark-field XTEM micrographs imaged using the 111 and 002 diffraction rings indicated by circles in the SAED pattern in (a).

$\simeq$4.1 nm. The selected-area electron diffraction (SAED) pattern in the inset of Fig. 7(a) was obtained with a 0.4 μm aperture centered at the midpoint of the film. It contains segments of 111, 002, and 022 diffraction rings. However, the primary diffracted intensity along the growth direction emanates from 111-oriented grains, reflecting the strong texture of this film. The angular width of the 111 arcs, a measure of the mosaicity of 111-oriented columns, is $\pm 17°$, in good agreement with the full width at half maximum intensity, $\Gamma_\omega = 16.5°$, of the 111 XRD ω-rocking curve (not shown) from this layer.

Figures 7(c) and 7(d) are dark-field XTEM micrographs imaged using the circled portions of the 111 and 002 SAED ring segments, respectively, along the film growth direction. A comparison of the two dark-field images shows that while 111 and 002 grains coexist during the early stages of film growth, the 111 grains gradually overgrow the 002-oriented grains until at thicknesses $\gtrsim$150 nm, the film has a nearly complete 111 texture. The average column diameter $\langle d \rangle$ increases with increasing layer thicknesses from $<$10 nm at the film/substrate interface to $\simeq$37 nm at a film thickness of 500 nm. These observations indicate that there is a continuous competition between evolving 111- and 002-oriented columns.

Based upon density and TEM/XTEM analyses for 111-oriented layers, we attribute the tensile stress (Fig. 4) in these layers to a combination of differential thermal contraction and grain boundary relaxation.[31] The latter arises from the difference between grain boundary and surface energies along intercolumnar boundaries. The interatomic forces across closely spaced open boundaries are attractive giving rise to tensile strain due to adhesion at the film/substrate interface.

Figure 8(a) is a bright-field XTEM micrograph from an 002 δ-TaN sample. The microstructure is also columnar, but in this case fully dense in agreement with plan-view TEM results in Fig. 6(b) and film density measurement results in Fig. 5. The surface is significantly smoother, with a rms roughness of $\simeq$2.7 nm, than 111-textured layers. The inset in Fig. 8(a) is a SAED pattern exhibiting strong 002 and weak 111 reflections along the growth direction. The angular length of the 002 arcs is $\pm 10°$, consistent with the 002 XRD ω-rocking curve width, $\Gamma_\omega = 9.4°$.

The dark-field images in Figs. 8(b) and 8(c), obtained using the circled portions of the 002 and 111 SAED ring segments along the film growth direction, show that microstructure evolution in δ-TaN layers grown with high J_i/J_{Ta} values also involves competitive growth. Both 002 and 111 grains are present at film thicknesses up to $\simeq$200 nm. In this

Downloaded 31 Oct 2002 to 128.113.37.128. Redistribution subject to AIP license or copyright, see http://ojps.aip.org/japo/japcr.jsp

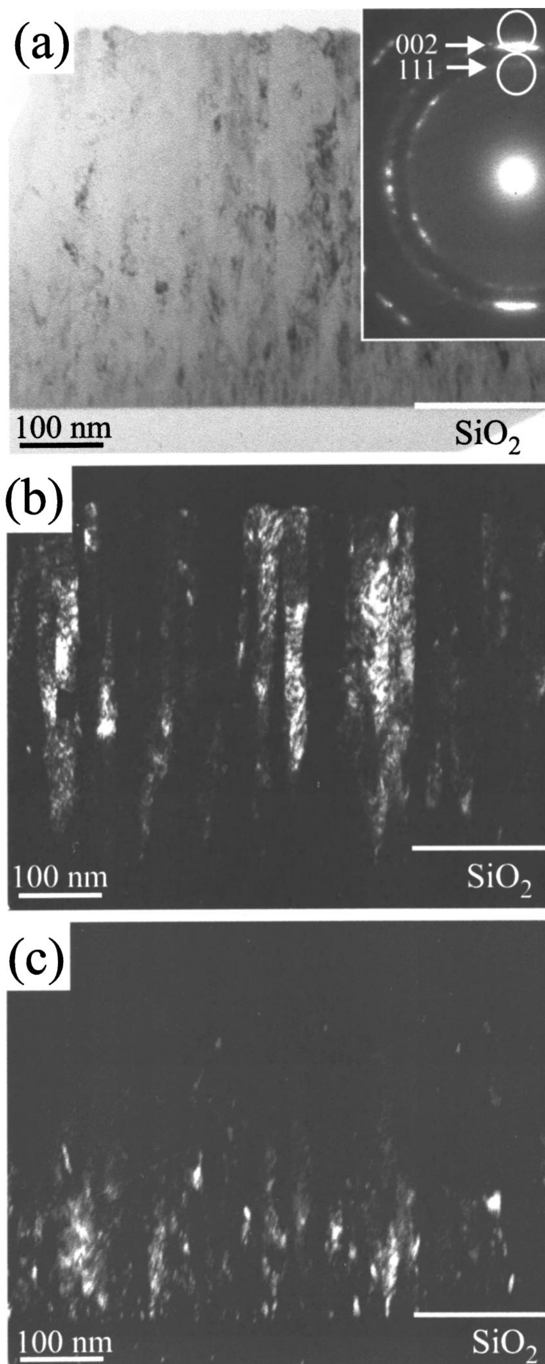

FIG. 8. (a) Bright-field XTEM micrograph and corresponding SAED pattern obtained from the sample corresponding to Fig. 6(b). (b) and (c) are dark-field XTEM micrographs imaged using 002 and 111 diffraction rings indicated by circles in the SAED pattern in (a).

case, however, it is the 002 columns that win by overgrowing the 111 columns. The average column diameter as a function of thickness is approximately the same as for 111-oriented layers.

We attribute the small compressive stress in the 002-oriented layers (see Fig. 4) grown with high ion irradiation to the presence of residual lattice damage, generated by ion irradiation-induced recoil and implantation events, which cannot be fully annealed out during low-temperature deposition. This assignment is consistent with the continuous in-

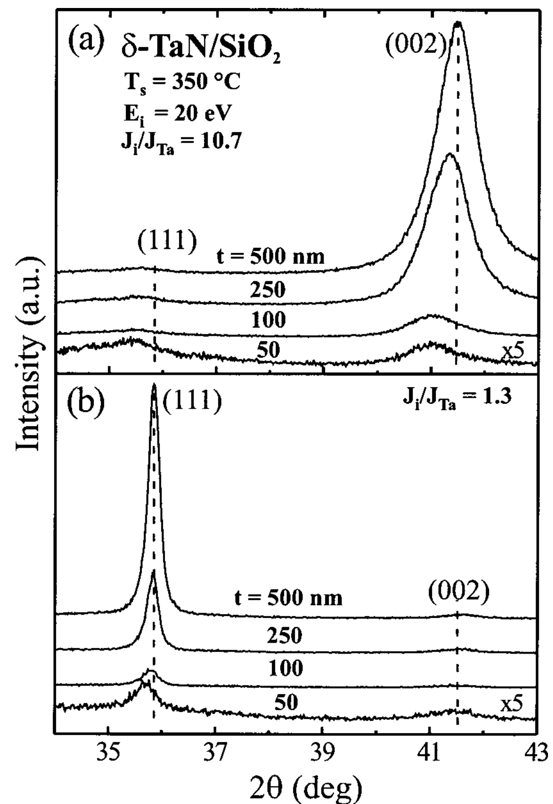

FIG. 9. XRD ω–2θ scans from TaN layers deposited on amorphous SiO_2 at 350 °C as a function of film thickness t. E_i was maintained constant at 20 eV: (a) $J_i/J_{Ta}=10.7$ and (b) $J_i/J_{Ta}=1.3$.

crease in $a_\perp$ values for 002-oriented layers grown with $J_i/J_{Ta}>6.6$.

In order to probe the pathway for texture evolution in more detail, we have grown $E_i=20$ eV δ-TaN layers with $J_i/J_{Ta}=1.3$ and 10.7 to thicknesses t ranging from 50 to 500 nm. Figure 9 shows XRD ω–2θ scans as a function of t. With both ion fluxes, the 50-nm-thick layers exhibit mixed orientations. As film thicknesses are increased, the dominant preferred orientations, 111 with $J_i/J_{Ta}=1.3$ and 002 with $J_i/J_{Ta}=10.7$, develop gradually. Both (111) and (002) peak positions in Fig. 9 are shifted to higher 2θ angles (i.e., decreasing $a_\perp$) with increasing layer thickness. $a_\perp^{002}$ for the layers grown with $J_i/J_{Ta}=10.7$ ranges from 0.4402 nm with $t=50$ to 0.4361 nm at $t=500$ nm while $a_\perp^{111}$ ($J_i/J_{Ta}=1.3$) varies from 0.4350 to 0.4344 nm over the same film thickness range. σ values obtained from XRD $\sin^2\psi$ measurements decrease from $+1.6$ and -2.0 GPa for 250-nm-thick 111- and 002-textured layers to $+1.4$ and -0.7 GPa for 500-nm-thick layers. We attribute this to partial relaxation of ion-irradiation-induced lattice damage in compressively strained layers during longer deposition times at T_s and to the increase in column size with increasing film thickness resulting in smaller open grain boundary area in tensile films.

IV. DISCUSSION

The results presented in Sec. III B show that the energy and flux of ions incident at the growing film during low-temperature reactive magnetron sputter deposition of TaN in

Downloaded 31 Oct 2002 to 128.113.37.128. Redistribution subject to AIP license or copyright, see http://ojps.aip.org/japo/japcr.jsp

mixed Ar/N_2 discharges are key parameters in determining film phase composition and microstructural evolution. An ion energy E_i of 20 eV is highly effective for controlling film microstructure, texture, and density through variations in J_i/J_{Ta} during growth of single-phase NaCl-structure δ-TaN without introducing large residual stresses. In contrast, 8.5 eV ion irradiation, even with high ion fluxes ($J_i/J_{Ta} = 10.7$), does not provide sufficient momentum transfer to overcome kinetic barriers for N_2 dissociation [≃9.8 eV (Ref. 32)] and adatom surface transport and, hence, results in δ-TaN_x layers with mixed orientation. Layers grown at $E_i = 30$ eV are two-phase mixtures consisting of cubic δ-TaN and the equilibrium hexagonal ε-TaN phase.

Increasing the incident ion-to-Ta flux ratio J_i/J_{Ta} from 1.3 to 10.7 while maintaining E_i constant at 20 eV during deposition at $T_s = 350\,°C$ ($T_s/T_m \simeq 0.19$) dramatically and selectively alters the properties of single-phase δ-TaN layers without affecting the composition. The N/Ta ratio remains constant at 1.13 ± 0.03. Predominantly 111- and 002-oriented islands are observed during the earliest stages of deposition. Following coalescence, grain growth is highly competitive as one orientation wins while the other dies out over layer thicknesses$\lesssim$200 nm. The upper part of 500-nm-thick layers exhibit a nearly complete 111-texture for growth with $J_i/J_{Ta} \leqslant 6.3$, whereas they have an essentially complete 002 texture with $J_i/J_{Ta} \geqslant 7.4$, and a mixed texture at intermediate ion-to-metal ratios. 111-oriented layers are underdense, contain both inter- and intracolumnar voids, and have very rough surfaces. In contrast, 002-oriented layers are fully dense with much smoother surfaces.

An early model[33] for ion-irradiation-induced texture modification during film growth proposed that layer orientation evolves toward grains with open channel directions. This allows the ion energy to be distributed over larger depths giving rise to lower sputtering yields than for grains with more densely packed orientations. Based upon such a model, increasing J_i/J_{Ta} should result in a tendency toward 002 texture, the most open orientation in the NaCl structure. Although this is, in fact, the trend we observe experimentally during δ-TaN deposition with $E_i = 20$ eV, TRIM simulations show that the sputtering yields of 20 eV Ar^+ and $N_2{}^+$ ions bombarding TaN are far too low to have any significant effect on film texture development. Moreover, we measure no change in film growth rate as a function of J_i/J_{Ta}. Thus, this model does not explain our results.

Pelleg, Zevin, and Lungo,[34] and later Oh and Je,[35,36] utilized thermodynamic arguments in an attempt to explain ion-induced texture development in reactive magnetron sputter deposited polycrystalline TiN layers. They proposed that the orientation should initially be 002, corresponding to the lowest energy surface,[37] then evolve toward 111 with increasing thickness as the film develops ion-irradiation-induced compressive stress. The 111 texture becomes favored at higher stress levels since the elastic modulus of TiN is lower in the [111] direction. The change in orientation in this model is driven by the film/substrate system minimizing the total free energy. However, our results for δ-TaN show exactly the opposite effect. 111-oriented layers exhibit tensile strain while 002 layers are under slight compression. Moreover, the texture of δ-TaN evolves from 111 toward 002 with increasing J_i/J_{Ta} suggesting that the transition is kinetically, rather than thermodynamically, controlled.

Results consistent with those reported here, in which the higher-energy surface emerges under low-temperature, low-ion-irradiation deposition conditions, have been reported for experiments involving TiN,[12,13] $Ti_{0.5}Al_{0.5}N$,[10] and ScN,[38] as well as for Monte Carlo simulations of fcc film growth.[39] In each of these cases, the results can be explained as being due to anisotropies in surface diffusivities and adatom potential energies. That is, the average adatom residence time is significantly higher at lattice sites on low-diffusivity (low-potential energy) versus high-diffusivity (high-potential energy) surfaces. Thus, adatoms that are stochastically deposited near grain boundaries and, through surface diffusion, sample sites on both sides of the boundary have a higher probability of becoming incorporated at the low-diffusivity surface which provides the more-stable, lower-potential-energy sites. Conversely, adatoms on high-diffusivity planes have larger mean-free paths with correspondingly higher probabilities to move off the plane and become trapped on adjacent grains. Thus, at low homologous deposition temperatures, grains with low surface diffusivities grow at the expense of their neighbors.

For the growth of TM nitrides by reactive sputter deposition, the interplay and competition among several interrelated surface reaction and diffusional processes determine film growth kinetics, surface morphology, film microstructure, and texture. The rate-limiting step for TM nitride film growth is cation incorporation which, in the present experiments, proceeds at a rate of 3 ML s^{-1}. The N_2 supply rate is much larger, $>10^3$ ML s^{-1}. If N_2 molecules reach Ta adatoms not yet incorporated in the lattice, they undergo dissociative chemisorption. However, all other incident N_2 molecules only physisorb on δ-TaN and desorb at kinetic rates with estimated lifetimes of $\simeq 10^{-9}$ s. This results in (001) surfaces that exhibit an essentially bulk-terminated structure with equal cation and anion number densities while 111 surfaces are fully N terminated. Ta adatoms form one N backbond on (001) surfaces and three N backbonds on (111) surfaces. Thus, cation diffusivities and potential energies are higher on 001-oriented grains than on 111 grains and Ta adatoms, following the arguments given above, have a larger chance of becoming trapped at 111 sites. Consequently, 111 grains will slowly and inexorably expand at the expense of the 002 grains under low-ion-flux growth conditions, as we observe.

However, as the incident ion-to-metal flux ratio in our experiments is increased from $J_i/J_{Ta} = 1.3$ to $\geqslant 7.4$, we observe a dramatic switch from 111 preferred orientation to the development of a complete 002 texture. This can be understood based upon the following mechanistic reaction path. Incident 20 eV N_2^+ ions are collisionally dissociated and provide a continuous source of atomic N which can chemisorb on 001 grains ([001] is a nonpolar direction in the NaCl structure), but not on N-terminated 111 grains. This is in contrast to incident thermal N_2 species which, as discussed above, have very short lifetimes on both surfaces in the absence of Ta adatoms. Thus, increasing J_i/J_{Ta} corresponds to

Downloaded 31 Oct 2002 to 128.113.37.128. Redistribution subject to AIP license or copyright, see http://ojps.aip.org/japo/japcr.jsp

raising the steady-state N coverage θ_N on 001 grains while θ_N remains at a constant N-terminated value on 111 grains. This has the important consequence of decreasing cation mean-free paths on (001) surfaces due to capture by N adatoms to form TaN_i ($i=1-4$) admolecules, which are more strongly bonded to the surface than Ta adatoms, and therefore have lower mobilities. That is, in the presence of an atomic N source, Ta adatoms on the (001) surface can form up to five bonds (four with in-plane N atoms and 1 N backbond), which decreases the effective 001 adatom potential energy below that on the 111. Consequently, the net flux of cations from 002 to 111-oriented grains is reversed under high-N_2^+-flux conditions, resulting in the development of 002 texture.

We also note that even in the absence of the ion-induced surface chemistry effects discussed above, momentum transfer due to ion irradiation during film growth has the general effect of increasing surface mobilities on all orientations,[40] resulting in a tendency, just as in the case of increasing deposition temperature, for texture evolution towards the thermodynamically lowest-energy surface, the (001).

In addition to the change in texture, from 111 to 002, with increasing ion-flux, we observe a corresponding increase in layer density and a decrease in surface roughness from underdense δ-TaN layers with both inter- and intragranular voids and self-organized growth mounds separated by deep surface trenches to fully dense layers with relatively smooth surfaces. We attribute the underdense microstructure of the low-temperature 111-textured layers to the presence of a higher Ehrlich barrier, due to the polar bilayer nature of steps on the 111 surfaces, for the migration of mobile species over down steps. This, combined with the large non-normal distribution of deposition flux inherent to sputtering,[41] causes strong persistent atomic shadowing, which exacerbates the rate of kinetic surface roughening and results in the subsequent formation of surface cusps and extended voids. In contrast, smaller Ehrlich barriers on (001) surfaces lead to smoother surfaces with less atomic shadowing and, hence, dense microstructures in 002-oriented layers. Increased adatom surface mobilities due to ion-irradiation-induced momentum transfer also play a role in the development of dense layers.

V. CONCLUSIONS

We have demonstrated that independently varying E_i and J_i/J_{Ta} during the low-temperature growth of polycrystalline δ-TaN layers by UHV magnetically unbalanced reactive magnetron sputter deposition in mixed Ar/N_2 discharges results in distinctly different mechanistic pathways for surface morphological and bulk microstructural evolution. The process window to control preferred orientation in δ-TaN layers, even with a high ion-to-metal flux ratio ($J_i/J_{Ta} = 10.7$), is relatively narrow as a function of E_i due to phase separation at incident ion energies $E_i \gtrsim 30$ eV and insufficient energy deposition per ion at low energies, $E_i = 8.5$ eV. With $E_i = 20$ eV, texture can be varied controllably and selectively by increasing J_i/J_{Ta} from 1.3 to $\gtrsim 7.4$.

Texture development is competitive with both 111 and 002 grains nucleating initially, irrespective of J_i/J_{Ta}. Preferred orientation then evolves with increasing film thickness to 111 with low J_i/J_{Ta} and 002 with high J_i/J_{Ta} values. The competition between 111- and 002-oriented grains is driven by strong anisotropies in potential energies and diffusivities of mobile surface species. At low J_i/J_{Ta}, (111) surfaces provide cation sites which are more stable than those on (001) surfaces, yielding a net cation flux from 002 to 111 oriented grains. In contrast, the use of high J_i/J_{Ta} values reverses the net flux due to lower effective cation adatom potential energies associated with increased steady-state atomic N coverages, deriving from collisionally induced dissociation of 20 eV N_2^+ ions, on (001) surfaces. In addition, the change from 111 to 002 preferred orientation leads, due to the combination of lower-step-edge Ehrlich barriers on the 001 surface with ion-irradiation-enhanced surface mobilities, to a transition from highly underdense 111-oriented δ-TaN layers with rough surfaces consisting of arrays of growth mounds separated by deep trenches, to layers with much smoother surfaces and fully dense 002-oriented microstructures.

ACKNOWLEDGMENTS

The authors gratefully acknowledge the financial support of the Department of Energy, Division of Materials Science, under Contract No. DEFG02-91ER45439 during the course of this research. The authors also appreciate the use of the facilities of the Center for Microanalysis of Materials, which is partially supported by DOE, at the University of Illinois. One of the authors (C.S.S.) is partially supported by Hynix Semiconductor, Inc., Ichon, Korea. One of the authors (N.H.) acknowledges the support from the Swedish Foundation for International Cooperation in Research and Higher Education (STINT).

[1] J.-E. Sundgren and H. T. G. Hentzell, J. Vac. Sci. Technol. A **4**, 2259 (1986).
[2] R. F. Bunshah and C. V. Deshpandey, Vacuum **39**, 955 (1989).
[3] J.-S. Chun, I. Petrov, and J. E. Greene, J. Appl. Phys. **86**, 3633 (1999).
[4] T. B. Massalski, in *Binary Alloy Phase Diagrams*, edited by T. B. Massalski (ASM International, Metals Park, OH, 1990), p. 2703.
[5] N. Terao, Jpn. J. Appl. Phys. **10**, 248 (1971).
[6] J. E. Greene, S. A. Barnett, J. E. Sundgren, and A. Rockett, in *Ion Beam Assisted Film Growth*, edited by T. Itoh (Elsevier, Amsterdam, 1988), Chap. 5.
[7] J. E. Greene, S. A. Barnett, J.-E. Sundgren, and A. Rockett, *Plasma Surface Interactions and Processing of Materials*, edited by O. Auciello, A. Gras-Marti, J. A. Valles-Abaraca, and D. L. Flamm, NATO ASI Series (Kluwer Academic, Amsterdam, 1990), p. 281.
[8] I. Petrov, L. Hultman, J.-E. Sundgren, and J. E. Greene, J. Vac. Sci. Technol. A **10**, 265 (1992).
[9] G. Håkansson, J.-E. Sundgren, D. McIntyre, J. E. Greene, and W.-D. Münz, Thin Solid Films **153**, 55 (1987).
[10] F. Adibi, I. Petrov, J. E. Greene, L. Hultman, and J.-E. Sundgren, J. Appl. Phys. **73**, 8580 (1993).
[11] I. Petrov, F. Adibi, J. E. Greene, W. D. Sproul, and W.-D. Münz, J. Vac. Sci. Technol. A **10**, 3283 (1992).
[12] J. E. Greene, J.-E. Sundgren, L. Hultman, I. Petrov, and D. B. Bergstrom, Appl. Phys. Lett. **67**, 2928 (1995).
[13] L. Hultman, J.-E. Sundgren, J. E. Greene, D. B. Bergstrom, and I. Petrov, J. Appl. Phys. **78**, 5395 (1995).
[14] I. Petrov, F. Adibi, J. E. Greene, L. Hultman, and J.-E. Sundgren, Appl. Phys. Lett. **63**, 36 (1993).

Downloaded 31 Oct 2002 to 128.113.37.128. Redistribution subject to AIP license or copyright, see http://ojps.aip.org/japo/japcr.jsp

[15] D. Gall, I. Petrov, N. Hellgren, L. Hultman, J.-E. Sundgren, and J. E. Greene, J. Appl. Phys. **84**, 6034 (1998).
[16] Updated version of the original TRIM program: see, for example, J. Ziegler, J. A. Biersack, and U. Litmark, *The Stoping Ranges of ions in Matter* (Pergamon, New York, 1985).
[17] J. H. Jeans, *The Dynamical Theory of Gases* (Dover, New York, 1956).
[18] A. V. Phelps, J. Phys. Chem. Ref. Data **20**, 557 (1991).
[19] L. R. Doolittle, Nucl. Instrum. Methods Phys. Res. B **9**, 344 (1993).
[20] I. Petrov, A. Myers, J. E. Greene, and J. R. Abelson, J. Vac. Sci. Technol. A **12**, 2846 (1994).
[21] B. Chapman, *Glow Discharge Processes* (Wiley, New York, 1980).
[22] C.-S. Shin, D. Gall, Y.-W. Kim, P. Desjardins, I. Petrov, J. E. Greene, M. Odén, and L. Hultman, J. Appl. Phys. **90**, 2879 (2001).
[23] T. B. Massalski, in *Binary Alloy Phase Diagrams*, edited by T. B. Massalski (ASM International, Metals Park, OH, 1990), p. 2703.
[24] C.-S. Shin, D. Gall, P. Desjardins, A. Vailionis, H. Kim, I. Petrov, J. E. Greene, and M. Odén, Appl. Phys. Lett. **75**, 3808 (1999).
[25] The Poisson ratio ν for TaN is not known. However, ν values for related cubic transition-metal nitrides vary only from 0.211 for TiN [J. O. Kim, J. D. Achenbach, P. B. Mirkarimi, M. Shinn, and S. A. Barnett, J. Appl. Phys. **72**, 1805 (1992)] to 0.29 for CrN [U. Wiklund, M. Bromark, M. Larsson, P. Hedenqvist, and S. Hogmark, Surf. Coat. Technol. **91**, 57 (1997)]. We used an average value of 0.25 for the calculation of a_o.
[26] *Encyclopedia of Inorganic Chemistry, Nitrides*, edited by R. B. King (Wiley, Chichester, 1984), Vol. 5, p. 2498.
[27] *Quick Reference Manual for Silicon Integrated Circuit Technology*, edited by W. E. Beadle, J. C. C. Tsai, and R. D. Plummer (Wiley, New York, 1994), p. 2–56.
[28] *Inorganic Index to Powder Diffraction File* (Joint Committee on Powder Diffraction Standards, Pennsylvania, 1997): Card No. 32-1283.
[29] D. Gerstenberg and C. J. Calbick, J. Appl. Phys. **35**, 402 (1964).
[30] D. J. Willmott, J. Appl. Phys. **43**, 4854 (1972).
[31] J. E. Greene, Crit. Rev. Solid State Mater. Sci. **17**, 547 (1992).
[32] *Handbook of Chemistry and Physics*, 78th ed., edited by D. R. Lide (CRC, New York, 1997/1998).
[33] D. Dobrev, Thin Solid Films **92**, 41 (1982).
[34] J. Pelleg, L. Z. Zevin, and S. Lungo, Thin Solid Films **197**, 117 (1991).
[35] U. C. Oh and J. H. Je, J. Appl. Phys. **74**, 1692 (1993).
[36] J. H. Je, D. Y. Noh, H. K. Kim, and K. S. Liang, J. Appl. Phys. **81**, 6126 (1997).
[37] L. Hultman, J.-E. Sundgren, and J. E. Greene, J. Appl. Phys. **66**, 536 (1989).
[38] D. Gall, I. Petrov, L. D. Madsen, J.-E. Sundgren, and J. E. Greene, J. Vac. Sci. Technol. A **16**, 2411 (1998).
[39] H. Huang, G. H. Gilmer, and T. D. Rubia, J. Appl. Phys. **84**, 3636 (1998).
[40] J. E. Greene, *Handbook of Crystal Growth*, edited by D. T. J. Hurle (Elsevier, Amsterdam, The Netherlands, 1993), Vol. 1, p. 639.
[41] Sputter deposition typically results in a $\cos(\theta)\sin(\theta)$ distribution, with θ being the polar angle, of the incoming atom flux. The highest flux, therefore, is at an azimuthal angle of 45°, as shown in Ref. 39.

Downloaded 31 Oct 2002 to 128.113.37.128. Redistribution subject to AIP license or copyright, see http://ojps.aip.org/japo/japcr.jsp